Irradiation-induced microstructural transformations in UO2 accelerated upon electronic energy deposition

Gaelle Gutierrez, Marion Bricout, Frederico Garrido, Aurélien Debelle, Laurent Roux, Claire Onofri-Marroncle

Irradiation-induced microstructural transformations in UO_2 accelerated upon electronic energy deposition

G. Gutierrez[1], M. Bricout[1], F. Garrido[2], A. Debelle[2], L. Roux[1], C. Onofri[3]*

[1] Université Paris-Saclay, CEA, Service de Recherches de Métallurgie Physique, 91191, Gif-sur-Yvette, France

[2] Université Paris-Saclay, CNRS, Laboratoire de Physique des 2 infinis Irène Joliot-Curie (IJCLab), 91405, Orsay, France

[3] CEA, DES, IRESNE, DEC, Cadarache, F-13108 St Paul lez Durance, France

Abstract

The combination of electronic and nuclear energy deposition may have a significant effect on the defect production and evolution. In nuclear reactor, the nuclear fuel is exposed to the irradiation of several particles such as the fission fragments (FF). Along their path, the ratio of electronic to nuclear energy loss evolves. To understand the impact of this coupling on the fuel microstructure, single and dual-beam ion irradiations of uranium dioxide (UO_2) were carried out. The damage evolution was investigated by Raman spectroscopy analysis correlated with Transmission Electronic Microscopy observations. A significant effect of electronic energy dissipation on defect formation and evolution was found, depending on the electronic energy loss level. With the increase of electronic energy loss, the microstructure evolution is even more pronounced.

Keywords: Uranium dioxide, Raman, TEM, Defects, Ionization, Dual ion beam irradiation

*Corresponding author

E-mail: gaelle.gutierrez@cea.fr

INTRODUCTION

Uranium dioxide (UO_2) is the common fuel used worldwide in pressurized water reactors and may be used in future generation IV reactors. The fission reaction of U^{235} after a neutron capture generates two fission fragments (FF) and neutrons. The majority of the energy produced by the fission reaction is transmitted to a light FF, typically Kr or Mo with an energy of 95 MeV, and to a heavy FF, I or Ba with an energy of 70 MeV [1]. The maximum electronic stopping power of FF is around 22 keV.nm^{-1}. For this kinetic energy range of projectiles, the electronic energy losses are predominant. At the atomic scale, ionizations and/or electronic excitations occur in the material. Under the effect of the FF slowing down, the ratio between electronic and nuclear energy losses evolves. The nuclear contribution increases inducing the production of atomic displacement cascades. One way to investigate the involved mechanisms without dealing with highly radioactive of the spent nuclear fuel is to perform ion beam irradiations. The behaviour of UO_2 depleted pellets under ion irradiations has been intensively studied at either low or high energy. In the low-energy regime, ions interact mainly with target nuclei through nuclear collisions, and the corresponding slowing-down regime is usually referred to as the nuclear energy-loss regime (S_n). In contrast, swift ions interact principally with target electrons, leading to excitations and ionizations, and ions mainly slow down by inelastic collisions in a regime usually called electronic energy-loss regime (S_e).

Low-energy ion irradiations lead to point defect formation from the early stage of irradiation [2-4]. The defect agglomeration induces the formation of dislocation loops and cavities nucleation [5-10]. High-energy ion irradiations could induce ion tracks along the ion paths [11-15]. The threshold value for the track formation in the electronic energy loss regime ranges from 22 to 29 keV.nm^{-1} [13]. However, at intermediate electronic stopping power (< 20 keV.nm^{-1}), only few data on the element diffusion under irradiations with swift heavy ions are available [16, 17]. Depending on materials, the ionization effects can lead to several processes [18, 19]. For example, amorphization along the ion path can occur in pure metals [20, 21] or in complex alloys [22, 23]. Furthermore, an annealing of pre-existing disorder under ionizing irradiation conditions is reported in some materials such as silicon and silicon carbide [24-27]. Moreover, the combination between electronic and nuclear energy deposition can also lead to synergistic damage production [28].

Recently, a coupling between the nuclear and electronic energy losses in UO_2 was demonstrated [29, 30]. However, the underlying mechanisms behind this phenomenon are currently studied and the effect of different parameters (flux, temperature) must be determined using separated effect studies. This work seeks to evaluate the influence of electronic energy deposition level on the ionization-induced recovery processes in UO_2. Single and dual-beam ion irradiations were carried out with different energies to monitor the electronic energy loss deposition. A combination between experiments, using Raman spectroscopy analysis and Transmission Electronic Microscopy (TEM) observations, and simulations, using inelastic thermal spike (iTS) model, was performed to provide insight on the phenomena. We show that electronic energy dissipation has a significant effect on defect formation and evolution depending on the electronic energy loss level.

EXPERIMENTAL METHODS

Sample preparation

Polycrystalline UO_2 pellets were sintered and cut into discs using a saw equipped with a diamond wire. After polishing, they were annealed under an Ar-H_2 (5%) atmosphere at 1973 K for 24 h. They were then mirror-polished with colloidal silica suspension to reduce effects due to grain boundaries, annealed under the same Ar-H_2 (5%) atmosphere at 1673 K for 4 h in order to maintain their stoichiometry (O/U = 2.00) and remove the last damage induced by polishing. The mean grain size was measured at 7.6 µm and the density at 97% of the theoretical one (i.e. 10.95 g.cm^{-3}).

Ion irradiation

UO_2 discs were irradiated at the JANNuS Saclay facility [31]. Irradiation temperature, 293 K, was monitored by thermocouples and by a thermal camera. Two single ion beam irradiations were performed with 900 keV I and 2 MeV Xe, referred to as S_n(I) and S_n(Xe). Three dual-ion irradiations were also carried out with 0.9 MeV I and 27 MeV Fe, 0.9 MeV I and 14 MeV Ar and 2 MeV Xe and 8.3 MeV Si ion beams, referred to as $(S_n\&S_e)_{high}$, $(S_n\&S_e)_{med}$ and $(S_n\&S_e)_{low}$, respectively. To minimize beam heating at the surface of disks, all ion fluxes were kept below 1×10^{11} cm^{-2}.s^{-1}. For the dual-ion beam irradiations, the ion fluences were increased up to 4×10^{14} and 8×10^{14} cm^{-2} for the S_n (I and Xe) and the S_e (low, mid and high) ion beams, respectively. A similar ratio between the irradiation fluence of low- and high-energy ions was applied for all the dual-ion beam irradiations. The irradiation conditions are reported in Table 1.

Sample denomination	Irradiation sequence	dE/dx_{elect} at surface	dpa max induced by S_n ion at 4×10^{14} cm^{-2}	Fluence ratio $\Phi(S_e)/\Phi(S_n)$
S_n(I)	Single ion beam : 900 keV I	0.3	2.7	-
S_n(Xe)	Single ion beam : 2 MeV Xe	0.5	3.0	-
$(S_n\&S_e)_{low}$	Dual ion beam : 2 MeV Xe and 8.3 MeV Si	6.0	3.0	2
$(S_n\&S_e)_{med}$	Dual ion beam : 0.9 MeV I and 14 MeV Ar	8.0	2.7	2
$(S_n\&S_e)_{high}$	Dual ion beam : 0.9 MeV I and 27 MeV Fe	12.0	2.7	2

Table 1: Ion irradiation parameters for single and dual-ion beam conditions in UO_2 samples: the irradiation sequences, the maximum displacements per atom (dpa) generated by the low-energy ion at 4×10^{14} cm^{-2}, the electronic stopping power (dE/dx_{elect}*) at the surface and the ratio between the high-energy (S_e) and the low-energy (S_n) ion fluence are reported.*

SRIM Simulations

SRIM calculations were performed using the full-damage cascade mode [32]. The threshold displacement energies of 40 and 20 eV are used for U and O, respectively [33, 34]. Note that, for the S_n(I) and S_n(Xe) irradiations, a similar value in term of displacements per atom (dpa) was achieved during the irradiations for the same ion fluence (Tab. 1). For the 27 MeV Fe, 14 MeV Ar and 8.3 MeV Si ions, electronic energy loss is predominant and nuclear energy loss can be neglected on the first micrometre (see Table 1 and Fig. 1), which is larger than the implantation depth of 0.9 MeV I and 2 MeV Xe ions (i.e. < 0.5 µm).

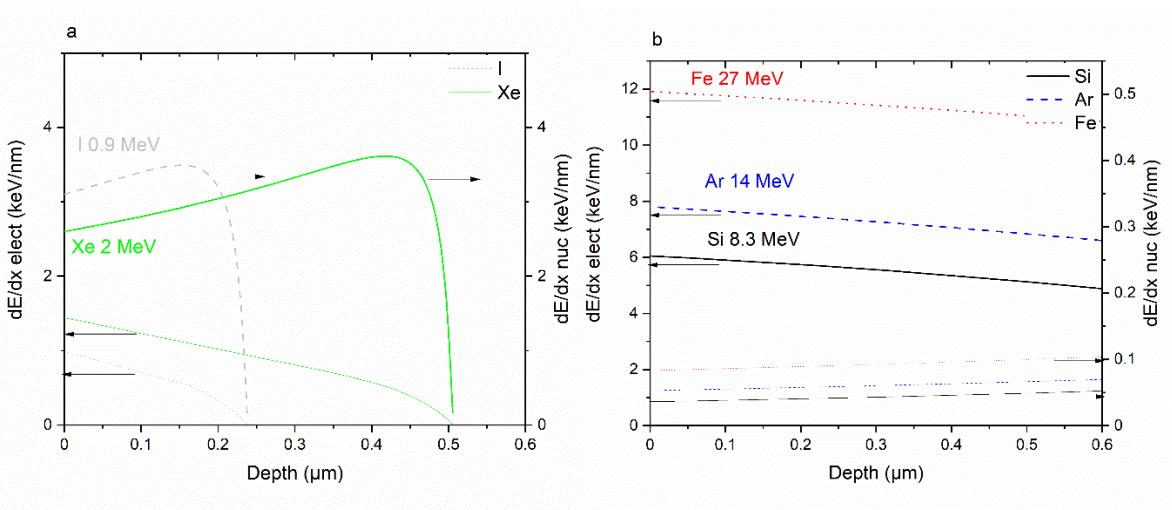

*Figure 1: Nuclear (*dE/dx$_{nuc}$*) and electronic (*dE/dx$_{elect}$*) stopping powers vs depth for UO_2 irradiated with (a) the S_n ions: 900 keV I and 2 MeV Xe and (b) the S_e ions: 8.3 MeV Si, 14 MeV Ar and 27 MeV Fe ions. Calculations were performed using the SRIM code [32]. The thicker lines correspond to the* dE/dx$_{nuc}$ *for the S_n ions and to the dE/dx$_{elect}$ for the S_e ions.*

Raman spectroscopy analysis

Raman analyses using an Invia Reflex Renishaw spectrometer coupled with a Leica microscope (x100) with a frequency-doubled Nd:YAG (532 nm) laser and a 2400 groove / mm grating were carried out on virgin and irradiated samples. A laser power less than 1 mW was used to avoid the UO_2 oxidation. The Raman spectrometer was calibrated with a silicon single crystal. In order to perform Raman measurements along the incident ion path, UO_2 cross-sections were prepared. Raman maps along a line with a step of 0.1 µm were performed. The fitting module of the WiRE Raman Spectroscopy software (Renishaw) was used for the spectra simulation assuming Voigt profiles. The accuracy on band position deduced from the spectrum simulation is estimated at ± 1 cm^{-1}.

Transmission Electronic microscopy characterization

TEM observations were performed with a Thermo Scientific Talos F200S TEM (point resolution of 0.19 nm and Field Emission Gun) operating at 200 kV at the LECA (Laboratoire d'Examens des Combustibles Actifs) in CEA Cadarache, France. Electron-transparent cross sectional thin foils were prepared by the

Focused Ion Beam (FIB) technique at CP2M (Centre Pluridisciplinaire de Microscopie électronique et de Microanalyse) in Marseille, France.

RESULTS

Raman spectra analysis

To study the coupled effect of nuclear and electronic energy losses for the dual-ion irradiations, we compared the result of S_n irradiation with the S_n&S_e irradiations at a similar S_n ion fluence (4×10^{14} cm^{-2}). We only consider the thickness where the two beams (S_n and S_e ions) overlap, corresponding to the S_n stopping area (< 0.5 µm). For the two single ion irradiations at 4×10^{14} cm^{-2} (corresponding to 2.7 and 3.0 dpa for the S_n(I) and S_n(Xe) irradiations, respectively), a comparable spectrum with close band intensities and widths is observed. It is consistent with previous results where a similar Raman spectrum was recorded for the same value of dpa for an irradiation with dominant nuclear energy loss [35]. To simplify, only the Raman results for S_n(I) are presented in this paper. All the Raman spectra exhibit the T_{2g} band at 445 cm^{-1} (black arrow) corresponding to the triply degenerated Raman active mode, typical of the fluorite-type structure [36]. Three other bands in the 500-700 cm^{-1} range denoted by U1 (~532 cm^{-1}), LO (~574 cm^{-1}) and U3 (~636 cm^{-1}), not observed or with a very low intensity for the unirradiated UO_2, are also revealed. These three bands are associated with the local disorder induced during irradiation in the UO_2 crystal [37-40]. They are related to the formation of atomic-scale defects. Because of a resonance effect, the LO band (grey arrow) is much more intense compared to the U1 and U3 bands [41]. The LO band is a Raman-forbidden mode in the perfect fluorite-type structure becoming active in the presence of defects due to a breakdown in the selection rules. Cross-sections of the irradiated samples were prepared in order to map the Raman signal as a function of the depth along the ion path (from the surface up to 600 nm); the corresponding maps are shown in Figure 2. Due to the laser spot size (~ 0.7 µm), each Raman spectrum will be a contribution of the studied area (where the two beams overlap) plus a part of the bulk (for S_n) or a sample part only irradiated with S_e ions (for S_n&S_e). For the low-energy ion irradiation (S_n), the LO band intensity is higher than the T_{2g} one. For the dual-ion beam irradiations, the ratio between T_{2g} and LO band intensities evolves with increasing dE/dx_{elect} of the high-energy ion: the LO band area decreases, while a slight T_{2g} band area increase is observed. A similar evolution to that LO band intensity is remarked for the U1 and U3 band intensities. This behaviour is related with the defect concentration evolution.

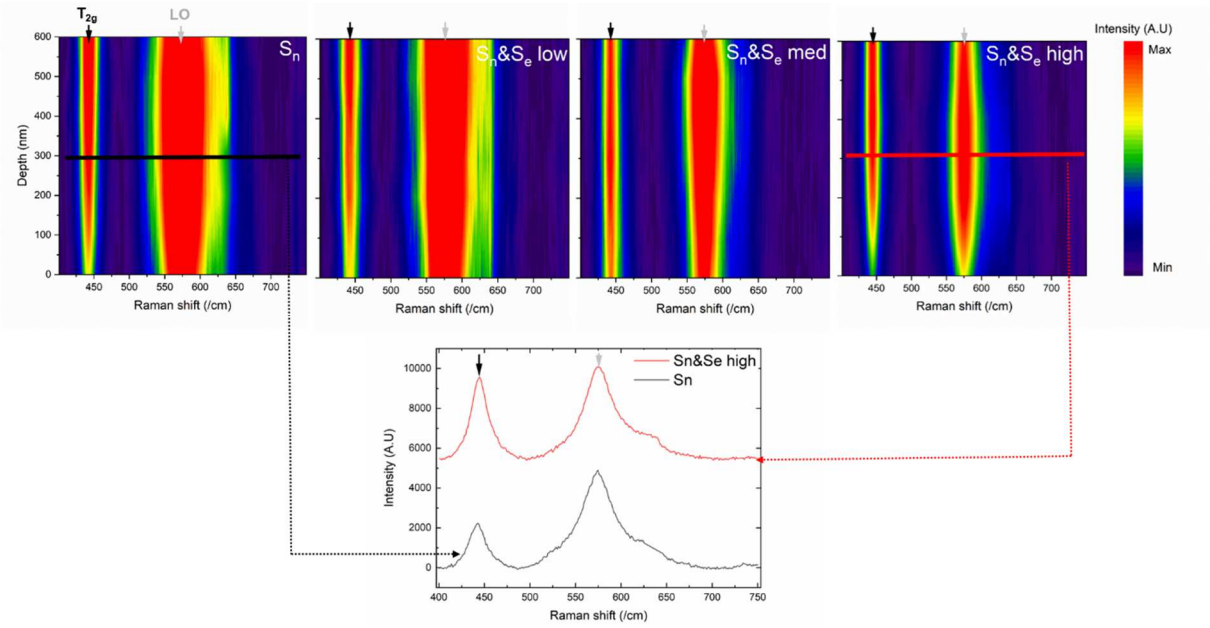

Figure 2: Raman mappings recorded on UO_2 cross section samples for the S_n(I) irradiation at a fluence of 4 × 10^{14} cm^{-2} and the dual-ion beam irradiations $(S_n\&S_e)_{low}$, $(S_n\&S_e)_{med}$ and $(S_n\&S_e)_{high}$ at a S_n fluence of 4 × 10^{14} cm^{-2} and S_e ion fluence of 8 × 10^{14} cm^{-2}. The bottom figure presents Raman spectrum of the S_n(I) and $(S_n\&S_e)_{high}$ irradiated samples at a depth of 300 nm. The lines on the Raman mappings of S_n(I) and $(S_n\&S_e)_{high}$ irradiations at a depth of 300 nm show where the Raman spectra are extracted.

To extract the LO area, the Raman spectra were fitted (Fig. 3). We used the Raman spectra measured at a depth of 300 nm (Fig. 2), where the laser probes the entire studied zone (two beams interaction) plus a part of virgin or high-energy irradiated sample. The LO band area for the $S_n\&S_e$ irradiations is compared with the LO area for the corresponding S_n irradiation. Therefore, the ratio is equal to 1 for the S_n irradiation. It decreases with the increase of dE/dx_{elect}. This result highlights that the local disorder in UO_2 is correlated to the level of the electronic energy loss.

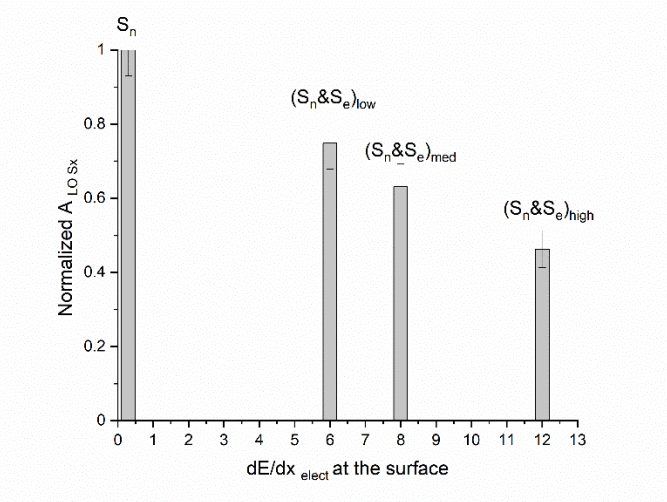

Figure 3: Ratio between the normalized LO band area for the performed irradiations and the LO band area for the corresponding S_n irradiation (S_n(I) or S_n(Xe)) (Normalized $A_{LO\,Sx}$) as function as the electronic stopping power of the high-energy ions (S_e) at the surface. The considered Raman spectra correspond to the spectra measured at a depth of 300 nm.

Transmission Electronic Microscopy observations

TEM samples were prepared using the FIB technique, a process that frequently generates disorder in the prepared lamella. Hence, we observed that, after the S_n(I) irradiation at 4 × 10^{14} cm^{-2}, the damage was similar to that observed in the lamella of the pristine crystal (see supplementary material). This result does not mean that no defects are formed by the 900 keV I irradiation. Indeed, extended defects (dislocation loops and cavities) are observed after ion irradiations at low fluences (around 10^{13} cm^{-2} corresponding to ~ 0.1 dpa) [29, 42]. Already at a fluence of 7 × 10^{14} cm^{-2}, more defects are detected in the irradiated sample than in the un-irradiated one. The microstructures induced by S_n(I) or S_n(Xe) are comparable in terms of loop density and size for an equivalent dpa value (see supplementary material). In contrast, after the S_n&S_e irradiations (either low, med or high), the microstructure appears dramatically different than the one observed after the sole S_n irradiation: a change in the loop density and/or the appearance of dislocation lines are clearly noted (see Fig. 4). The loop and line dislocation densities obtained for the S_n&S_e irradiations are compared with those for the S_n irradiations in Table 2.

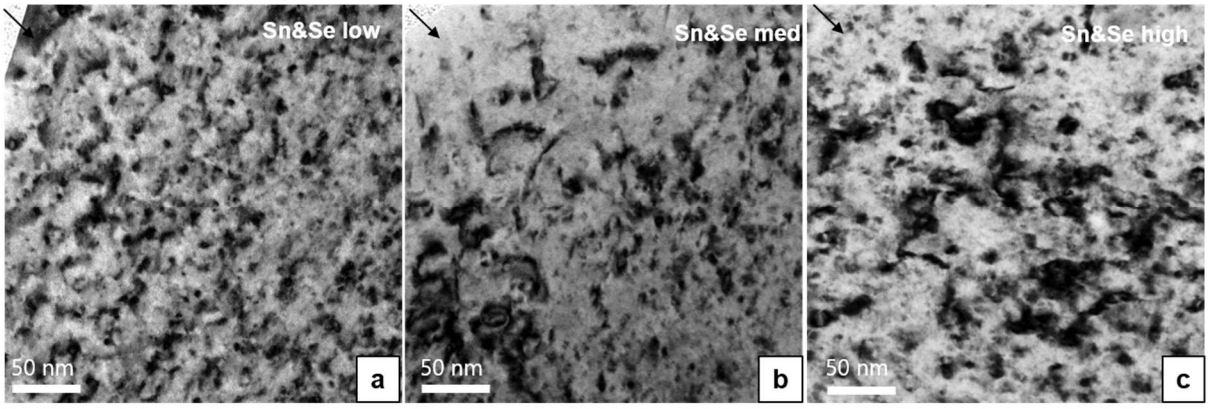

Figure 4: Bright field TEM micrographs of irradiated UO_2 samples under the (a) $(S_n\&S_e)_{low}$, (b) $(S_n\&S_e)_{med}$ and (c) $(S_n\&S_e)_{high}$ irradiations at a S_n fluence of 4 × 10^{14} cm^{-2} and S_e ion fluence of 8 × 10^{14} cm^{-2}. Arrows represent the implantation surface. The diffraction vector is along <220>.

In the S_n region (at a depth < 0.5 µm), the sample subjected to the $(S_n\&S_e)_{low}$ irradiation exhibits only dislocation loops (Fig. 4.a), but their density is tripled as compared to the sole S_n irradiation for a similar S_n ion fluence (4×10^{14} cm^{-2}) and more than doubled compared to the sole S_n irradiation with an ion fluence two times higher (7 × 10^{14} cm^{-2}). With increasing dE/dx_{elect}, i.e. for $(S_n\&S_e)_{med}$, dislocation lines start to appear, and no change in the loop density is observed. This loop density is maintained with further increase in dE/dx_{elect} (i.e. high regime), but the line density is, on the contrary, multiplied by ~5 (Fig. 4.b-c).

	Dislocation loop density (10^{16} loops.cm^{-3}) g = 220 reflection	Dislocation line density (10^{9} cm^{-2})
Un-irradiated	9.4 ± 1.4	-
S_n(I) at 4×10^{14} cm^{-2}	8.6 ± 1.4	-
S_n(Xe) at 7×10^{14} cm^{-2}	11.0 ± 2.6	-
S_n(I) at 7×10^{14} cm^{-2}	12.5 ± 2.6	-
$(S_n\&S_e)_{low}$	26.6 ± 6.7	-
$(S_n\&S_e)_{med}$	8.8 ± 2.2	2.6 ± 0.6
$(S_n\&S_e)_{high}$	8.0 ± 2.0	14.0 ± 3.0

Table 2: Dislocation loop and line densities as function of the irradiation conditions. The diffraction vector is along <220>.

The dislocation size distribution is shown in Figure 5. After the sole S_n irradiation at 7 × 10^{14} cm^{-2}, a majority of loops smaller than 5 nm are observed. After the $(S_n\&S_e)_{low}$ irradiation, only small changes compared to the S_n irradiation at 7 × 10^{14} cm^{-2} are revealed: loops smaller than 5 nm tends to increase a little (+ 5%) and few loops larger than 10 nm are also observed. In addition, the $(S_n\&S_e)_{high}$ irradiation induces a clear decrease in density of the smaller (< 5 nm) loops and an increase in the larger (> 5 nm) ones. The size distribution for the $(S_n\&S_e)_{med}$ irradiation presents a similar evolution as for the $(S_n\&S_e)_{high}$ irradiation but in smaller proportions.

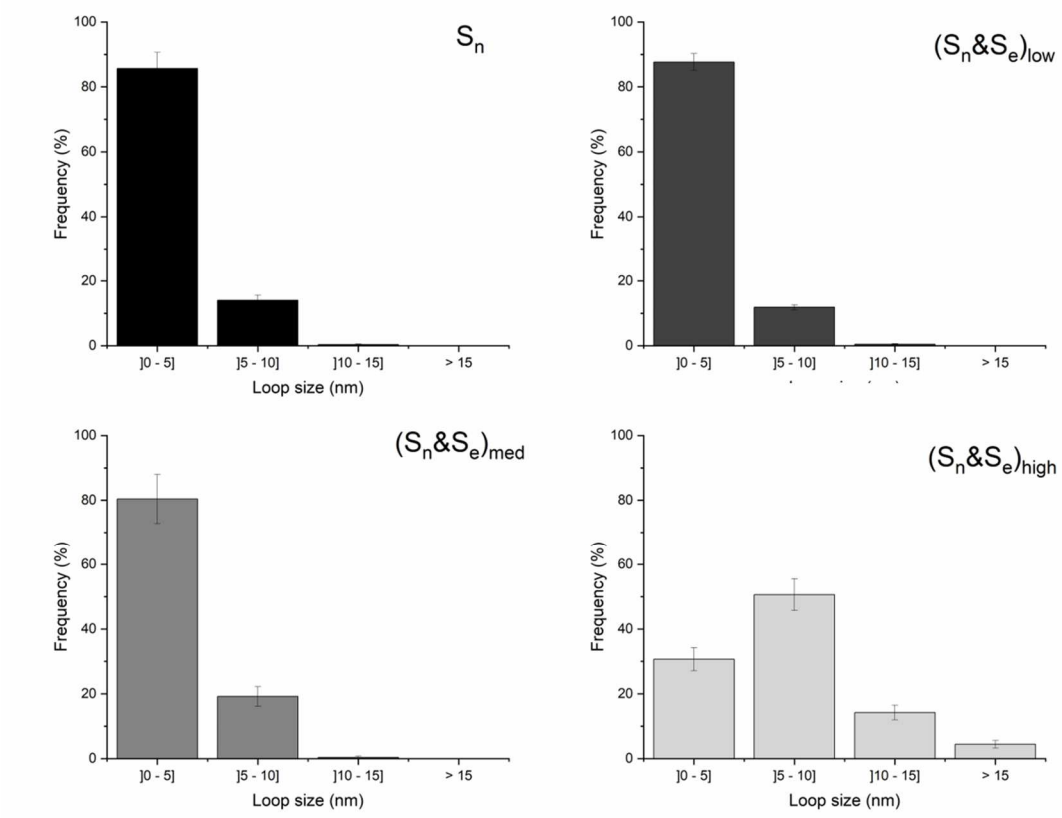

Figure 5: Loops size distribution of the UO_2 samples for the sole S_n irradiation at a fluence of 7 × 10^{14} cm^{-2} and the dual-ion beam irradiations $(S_n\&S_e)_{low}$, $(S_n\&S_e)_{med}$ and $(S_n\&S_e)_{high}$ at a S_n fluence of 4 × 10^{14} cm^{-2} and S_e ion fluence of 8 × 10^{14} cm^{-2}.

DISCUSSION

4.1 Effect of the dual-ion beam irradiation on the microstructure evolution

To investigate the coupled influence of ionization and damage on defect production, single and dual-beam ion irradiations were carried out. A significant effect of electronic energy dissipation on radiation-induced defect evolution with a strong dependence on electronic stopping power was revealed. It appears that the local disorder decreases with the increase of electronic energy deposition during simultaneous irradiations for an equivalent nominal nuclear damage level (around 3 dpa). This evolution (U1, LO and U3 bands) may be correlated to the formation of uranium point defects (interstitial or vacancy) through an indirect mechanism [40]. A decrease of the LO band intensity was also revealed after an annealing at 300°C [3]. Thus, the decrease of LO band intensity, after the S_n&S_e irradiations, can likely be ascribed to a decrease of uranium point defect concentration due to defect recombination/annihilation. In addition, the increase of electronic energy deposition enhances the formation and growth of the dislocation loops as illustrated on figure 6. The transformation of the loops into lines is even observed for the highest electronic stopping power value.

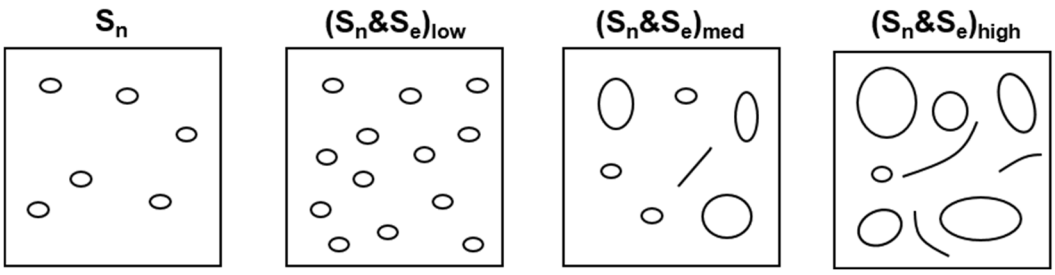

Fig. 6: Schematic view of the dislocations stage evolution depending on the irradiation conditions. The circles represent the dislocation loops and the lines the dislocation lines.

For the ballistic regime, with the fluence increase, dislocation loops are formed. They are then nucleated continuously and increase in number until the density saturation with the fluence increase (Fig. 7). The dislocation loop then grow in size: the smallest disappearing in favor of the larger ones. By geometric overlap, the loops evolve into dislocation line, inducing a reduction in terms of size and density. With the increase of irradiation temperature, the extended defects kinetic evolves. The dislocation loop growth is accelerated by the irradiation temperature increase (600°C) due to the mobility of the point defects [43].

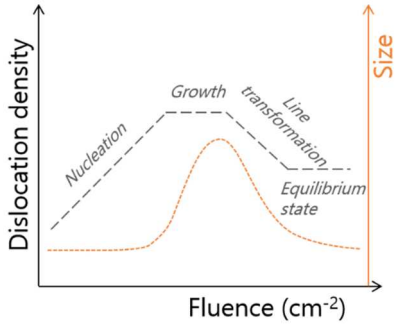

Figure 7: Schematic view of the dislocations evolution (density and size) according to the ion fluence.

For a dual-ion beam irradiation, the dislocation loop evolution is quite similar than for a single low-energy ion irradiation at room temperature: continuous small loop nucleation followed by dislocation loop growth and final evolution into dislocation line [29]. However, the dislocation loop evolution is accelerated under the dual-ion beam irradiation as compared to the sole low-energy irradiation as it is observed with the irradiation temperature increase.

4.2 Calculation of the deposited energy by the high-energy ion: iTS modelling

To estimate the deposited energy after the passage of the high-energy ions (27 MeV Fe, 14 MeV Ar and 8.3 MeV Si) during the S_n&S_e irradiations, the inelastic thermal spike (iTS) model was applied. This model was developed to account for mid-range ion energy, in which the temperature increase is calculated before reaching the melting temperature [44, 45]. Concerning the 27 MeV Fe and the 14 MeV Ar ions, the electronic stopping power is dominant. However, the nuclear stopping power is not completely negligible for the 8.3 MeV Si ions irradiation. As the ITS model was developed to calculate the thermal energy distribution for predominant electronic regime, the calculations can only give an order of magnitude for the deposited energy, not an absolute value. It considers that the kinetic energy of the incident high-energy ion is transferred to the atoms as thermal energy. In this process, the first step consists to an energy transmission from the incident ion to the target material electrons. The energy transfer, from the electron to the atomic network, occurs by electron-electron interactions then an electron-phonon coupling. The set of coupled equations (eq. 1 and eq. 2) describes this process:

$$C_e(T_e)\frac{dT_e}{dt} = \frac{1}{r}\frac{d}{dr}\left[rK_e(T_e)\frac{dT_e}{dr}\right] - g(T_e - T_a) + A(r,t) \qquad \text{Eq.1}$$

$$C_a(T_a)\frac{dT_a}{dt} = \frac{1}{r}\frac{d}{dr}\left[rK_a(T_a)\frac{dT_a}{dr}\right] + g(T_e - T_a) \qquad \text{Eq.2}$$

Where: T_e, T_a, C_e, C_a, K_e, K_a stand for the electronic and atomic temperatures, specific heats and thermal conductivities, r and t correspond to the radial distance and the time from the incident ion. A(r,t) is the distribution function of the incident ion energy deposition to the electronic sub-system for a radius r and a time t. The electron-phonon coupling constant g is linked to the electronic mean free path (λ) via the relation $g = K_e/\lambda^2$. The electronic mean free path has been chosen to be 4.5 nm based on the work of Wiss et al. [13].

The 2D distribution of the energy deposited to the target atoms by the swift ions is displayed in Figure 8. Both the time and the radial distance around the incident ion (radius) are plotted in Fig. 8.

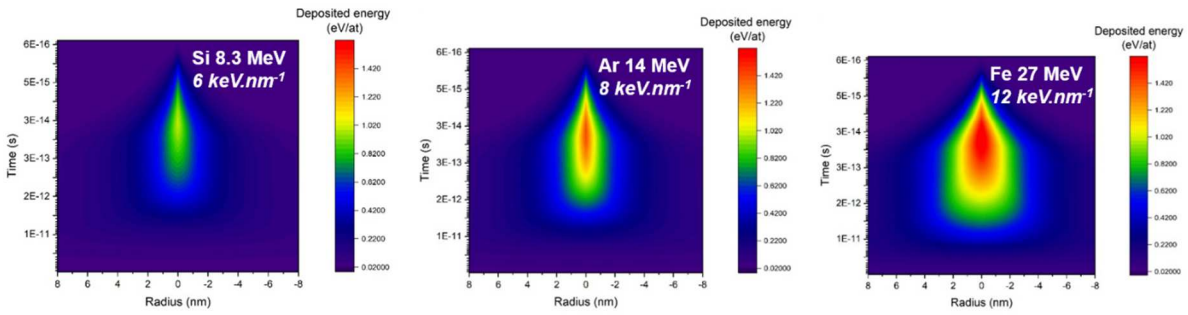

Figure 8: Deposited energy determined by iTS simulations after the passage of 8.3 MeV Si, 14 MeV Ar, and 27 MeV Fe ions. The x axis corresponds to the ion radius and the y axis to the time.

The comparison between the different cases reveals that:

- The melting energy (1.31 eV/at [46]) is reached only within a radius cylinder of 0.6 nm and for a time of 0.9 and 0.5 ps (equivalent to 9 and 5 atomic vibrations, respectively) for the 27 MeV Fe and 14 MeV Ar ions, respectively, corresponding to 9 and 5 atomic vibrations. However, this energy is never reached for the 8.3 MeV Si ions.
- For a fixed deposited energy of 0.6 eV/at, corresponding to the maximum energy achieved for Si ions during the minimum reliable time (1 ps), the 27 MeV Fe and the 8.3 MeV Si ions depose this energy during 3.5 ps in a radius of 3.4 nm and during 1 ps in a radius of 1.4 nm, respectively. Thus, even if the 8.3 MeV Si can depose a similar energy, it is for a shorter time and on a smaller volume.

Summarizing, the iTS simulations reveal that the highest electronic stopping power, the larger the energy deposited volume and the longer the deposition time. Furthermore, the melting energy can be reached during a very short time (< 1 ps) for the 27 MeV Fe and 14 MeV Ar ions, but not for 8 MeV Si ions.

4.2 Influence of electronic energy deposition level on the defect evolution

Our current TEM and Raman spectroscopy results indicate that the defect distribution (both in nature and size) induced by the S_n ions is affected by the electronic excitations generated by the S_e ions: both a decrease in the local disorder and a change in the extended defect characteristics (density and/or size) is clearly put forward upon simultaneous S_n&S_e irradiations.

The local disorder decrease, ascribed to a drop in the U point defect concentration, should be due to a short-range migration of those defects activated by the thermal load associated to the electronic energy deposition (see iTS). Those defects may then recombine or annihilate. This mechanism is enhanced with increasing the electronic stopping power. For the $(S_n\&S_e)_{low}$, in addition to this point defect annealing, the dislocation loop density is significantly increased, while the loop size is unchanged. This result also suggests a short-range migration of defects, but leading to defect clustering (clustering should be favored over recombination when the irradiation temperature is increased [47]). Therefore, a significantly larger loop nucleation rate can be expected upon dual beam irradiation, hence, the larger loop density observed for $(S_n\&S_e)_{low}$. When the electronic stopping power is further increased, the loop density remains unchanged (as compared to the sole S_n irradiation), but the average loop size is increased. Furthermore, dislocation lines appear, the density of which depends on dE/dx_{elect}: the higher dE/dx_{elect}, the larger the line density. This result suggests that with a higher deposited energy, the thermal load is enhanced, leading to the migration of different point defect and/or of small loop and their trapping at larger loops. It appears that the electronic energy loss induces an increase of defect recombination with a direct effect on the local disorder and an increase of defect clustering by the acceleration of loop kinetic.

Higher electronic energy deposition may induce the activation of defect migration as observed in SiC where the ionization-induced annealing of pre-existing defects is more efficient with increasing electronic stopping power of projectiles [26]. On pre-irradiated UO_2 samples, several thermal recovery stages were highlighted. A strain relaxation [48, 49] and a recovery of local disorder [3] occur that is attributed to the point defect recovery. A possible threshold of deposited energy is likely necessary to activate the migration of the different point defects. As the melting energy (1.31 eV/at) is reached only for the 27 MeV Fe and 14 MeV Ar ions ($(S_n\&S_e)_{high}$ and $(S_n\&S_e)_{med}$), a threshold of deposited energy could be reached and explain the observed acceleration of dislocation transformation from loops to lines.

4.4 Coupled effect of the electronic energy deposition and the defect spectrum on the microstructural evolution

The threshold of deposited energy also may depend on the defect size [26]. Indeed, high-energy ions interact with different defect types with variable sizes such as point defect (interstitial, vacancy) or extended one (clusters, loops, cavities). To precise the influence of electronic energy loss on the defect evolution, we compare the microstructure obtained after a sequential and simultaneous irradiation. It is worth stressing here to emphasize the difference between sequential and simultaneous irradiation conditions. Indeed, for the sequential irradiation condition, according to the initial S_n fluence, the high-energy ions interact mainly with already-created big defects (defect clusters, loops and cavities). Under dual-beam irradiation condition, the atomic configuration differs since an overlap of multiple sequential irradiations with very low fluence steps occur. The high-energy ions will thus continuously interact with small defects (point defects) and bigger defects (defect clusters, loops, cavities).

Thus, a pre-irradiated sample with S_n(I) ions (900 keV I) at 7×10^{14} cm^{-2} (corresponding to 4.7 dpa) presenting dislocation loops (mean loop dislocation diameter around 1.7 nm with a density of 12.2×10^{16} $loop.cm^{-3}$) was exposed to 27 MeV Fe ions (12 $keV.nm^{-1}$). As revealed on Figure 9, the TEM observations do not show dislocation lines (Fig. 9.b). However, the loop density decreases and their size increases after the 27 MeV Fe ion irradiation (mean loop dislocation diameter increases around 3.5 nm with a density of 7.4×10^{16} $loop.cm^{-3}$). Therefore, a dislocation loop growth occurs.

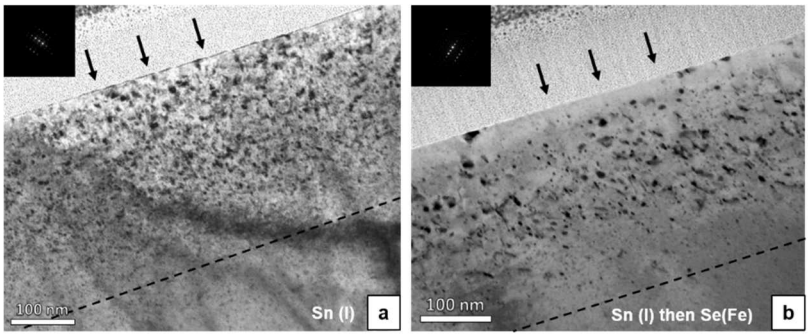

Figure 9: Bright field TEM micrographs of UO_2 samples (a) irradiated with 900 keV I ions (7×10^{14} cm^{-2}) (S_n(I)) and (b) pre-damaged by 900 keV I ions (7×10^{14} cm^{-2}) then irradiated with 27 MeV Fe ions (2×10^{15} cm^{-2}) (S_n(I) then S_e(Fe)). Arrows represent the implantation surface. The lines delimit the S_n stopping area. The diffraction vector is along <200>.

On the contrary, for a similar sequential irradiation but with a high-energy ion with a smaller dE/dx_{elect} (5 $keV.nm^{-1}$), no effect of electronic stopping on the defect evolution was observed [29]. This highlights that, at low electronic stopping power, dislocation loops are not directly affected by the high-energy ions. The deposited energy is not enough to induce a dislocation loop evolution. With the increase of dE/dx_{elect}, the ionization process affects the evolution of extended defects: the dislocation size increases and the density decreases.

In contrast, during simultaneous irradiations for similar electronic stopping power values (5 and 12 $keV.nm^{-1}$), the dislocation loops evolve for the two electronic stopping power levels. The difference observed between sequential and simultaneous irradiations points out that the microstructure evolution is not only linked to the electronic stopping power level but also to the defect kind (isolated point defect, extended one…) with whom the high-energy ion interacts. During the dual-beam irradiation, small defects (point defects) are continuously formed. Thus, even if there is no correlation in time and space between the S_n and S_e ions during the dual-beam irradiation, the S_e ions will then continuously interact with small defects. The deposited energy for the lower electronic stopping power (5 $keV.nm^{-1}$) may then be enough to activate the migration of some point defect. On contrary, only the deposited energy for the highest S_e ion (12 $keV.nm^{-1}$) induces an evolution of the extended defects. It could highlight the mobility activation of other defects (cluster, loop…) with the increase of electronic energy loss. Future systematic investigations are required to conclude on this point.

CONCLUSIONS

This work was devoted to the evaluation of the role of electronic stopping power on the ionization-induced recovery processes in UO_2. Single (S_n) and dual-beam (S_n&S_e) ion irradiations were performed at different energies at room temperature. Raman analysis and TEM observations were carried out to characterize the influence of electronic energy deposition. We show a clear effect of electronic energy dissipation on defect formation and evolution depending on the electronic energy loss level. The $(S_n\&S_e)_{low}$ irradiation leads to the creation of more dislocation loops with a similar size compared to the sole S_n irradiation. With the increase of dE/dx_{elect}, dislocation lines start to appear and dislocation loops grow, resulting in a decrease of the loop density and an increase of the loop size. Thus, due to the ionizations, radiation-induced defects continuously formed by the low-energy ion appear to be more mobile and favour dislocation loops growth by absorbing interstitial-type defects. The dislocation evolution kinetics is therefore accelerated. Moreover, electronic stopping power is not the only key parameter in the ionization-induced recovery processes. Indeed, for a sequential irradiation, the loop growth is not affected or decelerated for the corresponding dual-ion beam irradiation. Depending on the level of dE/dx_{elect}, the high-energy ion has an influence or not on the microstructure. This result points out a possible threshold in electronic energy loss coupled to the irradiation condition.

Acknowledgments

Authors acknowledge the JANNuS-Saclay facility staff for their help during the irradiations.

REFERENCES

[1] T. Wiss, A. Benedetti, E. De Bona, 2.05 - Radiation Effects in UO2☆, in: R.J.M. Konings, R.E. Stoller (Eds.), Comprehensive Nuclear Materials (Second Edition), Elsevier, Oxford, 2020, pp. 125-148.
[2] L. Desgranges, P. Simon, P. Martin, G. Guimbretiere, G. Baldinozzi, What Can We Learn From Raman Spectroscopy on Irradiation-Induced Defects in UO2?, JOM 66(12) (2014) 2546-2552.
[3] L. Desgranges, G. Guimbretière, P. Simon, F. Duval, A. Canizares, R. Omnee, C. Jégou, R. Caraballo, Annealing of the defects observed by Raman spectroscopy in UO2 irradiated by 25MeV He2+ ions, Nuclear Instruments and Methods in Physics Research Section B: Beam Interactions with Materials and Atoms 327 (2014) 74-77.
[4] R. Mohun, L. Desgranges, J. Léchelle, P. Simon, G. Guimbretière, A. Canizarès, F. Duval, C. Jegou, M. Magnin, N. Clavier, N. Dacheux, C. Valot, R. Vauchy, Charged defects during alpha-irradiation of actinide oxides as revealed by Raman and luminescence spectroscopy, Nuclear Instruments and Methods in Physics Research Section B: Beam Interactions with Materials and Atoms 374 (2016) 67-70.
[5] C. Onofri, M. Legros, J. Léchelle, H. Palancher, C. Baumier, C. Bachelet, C. Sabathier, Full characterization of dislocations in ion-irradiated polycrystalline UO2, Journal of Nuclear Materials 494 (2017) 252-259.
[6] B. Ye, A. Oaks, M. Kirk, D. Yun, W.-Y. Chen, B. Holtzman, J.F. Stubbins, Irradiation effects in UO2 and CeO2, Journal of Nuclear Materials 441(1) (2013) 525-529.
[7] L.F. He, J. Pakarinen, M.A. Kirk, J. Gan, A.T. Nelson, X.M. Bai, A. El-Azab, T.R. Allen, Microstructure evolution in Xe-irradiated UO2 at room temperature, Nuclear Instruments and Methods in Physics Research Section B: Beam Interactions with Materials and Atoms 330 (2014) 55-60.
[8] L.-F. He, M. Gupta, C.A. Yablinsky, J. Gan, M.A. Kirk, X.-M. Bai, J. Pakarinen, T.R. Allen, In situ TEM observation of dislocation evolution in Kr-irradiated UO2 single crystal, Journal of Nuclear Materials 443(1) (2013) 71-77.
[9] C. Onofri, C. Sabathier, C. Baumier, C. Bachelet, H. Palancher, B. Warot-Fonrose, M. Legros, Influence of exogenous xenon atoms on the evolution kinetics of extended defects in polycrystalline UO2 using in situ TEM, Journal of Nuclear Materials 512 (2018) 297-306.
[10] C. Onofri, C. Sabathier, C. Baumier, C. Bachelet, D. Drouan, M. Gérardin, M. Legros, Extended defect change in UO2 during in situ TEM annealing, Acta Materialia 196 (2020) 240-251.
[11] N. Ishikawa, T. Sonoda, T. Sawabe, H. Sugai, M. Sataka, Electronic stopping power dependence of ion-track size in UO2 irradiated with heavy ions in the energy range of ∼1MeV/u, Nuclear Instruments and Methods in Physics Research Section B: Beam Interactions with Materials and Atoms 314 (2013) 180-184.
[12] F. Garrido, C. Choffel, J.C. Dran, L. Thome, L. Nowicki, A. Turos, Structural modifications in uranium dioxide irradiated with swift heavy ions, Nuclear Instruments and Methods in Physics Research Section B: Beam Interactions with Materials and Atoms 127-128 (1997) 634-638.
[13] T. Wiss, H. Matzke, C. Trautmann, M. Toulemonde, S. Klaumünzer, Radiation damage in UO2 by swift heavy ions, Nuclear Instruments and Methods in Physics Research Section B: Beam Interactions with Materials and Atoms 122(3) (1997) 583-588.
[14] V.V. Pisarev, S.V. Starikov, Atomistic simulation of ion track formation in UO2, Journal of Physics: Condensed Matter 26(47) (2014) 475401.
[15] W.F. Cureton, R.I. Palomares, J. Walters, C.L. Tracy, C.-H. Chen, R.C. Ewing, G. Baldinozzi, J. Lian, C. Trautmann, M. Lang, Grain size effects on irradiated CeO2, ThO2, and UO2, Acta Materialia 160 (2018) 47-56.
[16] N. Djourelov, B. Marchand, H. Marinov, N. Moncoffre, Y. Pipon, N. Bérerd, P. Nédélec, L. Raimbault, T. Epicier, Study of temperature and radiation induced microstructural changes in Xe-implanted UO2 by TEM, STEM, SIMS and positron spectroscopy, Journal of Nuclear Materials 443(1) (2013) 562-569.
[17] L. Sarrasin, Y. Pipon, C. Gaillard, N. Moncoffre, N. Bérerd, P. Simon, D. Mangin, R. Ducher, R. Dubourg, Influence of temperature and electronic stopping power of UO2 irradiated with swift ions on Mo migration, Nuclear Instruments and Methods in Physics Research Section B: Beam Interactions with Materials and Atoms 435 (2018) 111-115.
[18] Y. Zhang, W.J. Weber, Ion irradiation and modification: The role of coupled electronic and nuclear energy dissipation and subsequent nonequilibrium processes in materials, 7(4) (2020) 041307.
[19] W.J. Weber, D.M. Duffy, L. Thomé, Y. Zhang, The role of electronic energy loss in ion beam modification of materials, Current Opinion in Solid State and Materials Science 19(1) (2015) 1-11.
[20] A. Dunlop, D. Lesueur, P. Legrand, H. Dammak, J. Dural, Effects induced by high electronic excitations in pure metals: A detailed study in iron, Nuclear Instruments and Methods in Physics Research Section B: Beam Interactions with Materials and Atoms 90(1) (1994) 330-338.

[21] C. Dufour, Z.G. Wang, M. Levalois, P. Marie, E. Paumier, F. Pawlak, M. Toulemonde, Sensitivity of metallic materials under irradiation with swift heavy ions, Nuclear Instruments and Methods in Physics Research Section B: Beam Interactions with Materials and Atoms 107(1) (1996) 218-222.
[22] A.A. Leino, G.D. Samolyuk, R. Sachan, F. Granberg, W.J. Weber, H. Bei, J. Liu, P. Zhai, Y. Zhang, GeV ion irradiation of NiFe and NiCo: Insights from MD simulations and experiments, Acta Materialia 151 (2018) 191-200.
[23] R. Sachan, M.W. Ullah, M.F. Chisholm, J. Liu, P. Zhai, D. Schauries, P. Kluth, C. Trautman, H. Bei, W.J. Weber, Y. Zhang, Radiation-induced extreme elastic and inelastic interactions in concentrated solid solutions, Materials & Design 150 (2018) 1-8.
[24] L. Thomé, G. Gutierrez, I. Monnet, F. Garrido, A. Debelle, Ionization-induced annealing in silicon upon dual-beam irradiation, J. Mater. Sci. 55(14) (2020) 5938-5947.
[25] L. Thomé, A. Debelle, F. Garrido, P. Trocellier, Y. Serruys, G. Velisa, S. Miro, Combined effects of nuclear and electronic energy losses in solids irradiated with a dual-ion beam, 102(14) (2013) 141906.
[26] Y. Zhang, H. Xue, E. Zarkadoula, R. Sachan, C. Ostrouchov, P. Liu, X.-l. Wang, S. Zhang, T.S. Wang, W.J. Weber, Coupled electronic and atomic effects on defect evolution in silicon carbide under ion irradiation, Current Opinion in Solid State and Materials Science 21(6) (2017) 285-298.
[27] R. Sachan, V.R. Cooper, B. Liu, D.S. Aidhy, B.K. Voas, M. Lang, X. Ou, C. Trautmann, Y. Zhang, M.F. Chisholm, W.J. Weber, Forging Fast Ion Conducting Nanochannels with Swift Heavy Ions: The Correlated Role of Local Electronic and Atomic Structure, The Journal of Physical Chemistry C 121(1) (2017) 975-981.
[28] E. Zarkadoula, K. Jin, Y. Zhang, W.J. Weber, Synergistic effects of nuclear and electronic energy loss in KTaO3 under ion irradiation, 7(1) (2017) 015016.
[29] M. Bricout, G. Gutierrez, C. Baumier, C. Bachelet, D. Drouan, F. Garrido, C. Onofri, Synergy of electronic and nuclear energy depositions on the kinetics of extended defects formation in UO2, based on in situ TEM observations of ion-irradiation-induced microstructure evolution, Journal of Nuclear Materials 554 (2021) 153088.
[30] M. Bricout, C. Onofri, A. Debelle, Y. Pipon, R.C. Belin, F. Garrido, F. Leprêtre, G. Gutierrez, Radiation damage in uranium dioxide: Coupled effect between electronic and nuclear energy losses, Journal of Nuclear Materials 531 (2020) 151967.
[31] S. Pellegrino, P. Trocellier, S. Miro, Y. Serruys, É. Bordas, H. Martin, N. Chaâbane, S. Vaubaillon, J.P. Gallien, L. Beck, The JANNUS Saclay facility: A new platform for materials irradiation, implantation and ion beam analysis, Nuclear Instruments and Methods in Physics Research Section B: Beam Interactions with Materials and Atoms 273 (2012) 213-217.
[32] J.F. Ziegler, M.D. Ziegler, J.P. Biersack, SRIM – The stopping and range of ions in matter (2010), Nuclear Instruments and Methods in Physics Research Section B: Beam Interactions with Materials and Atoms 268(11) (2010) 1818-1823.
[33] C. Meis, A. Chartier, Calculation of the threshold displacement energies in UO2 using ionic potentials, Journal of Nuclear Materials 341(1) (2005) 25-30.
[34] J. Soullard, High voltage electron microscope observations of UO2, Journal of Nuclear Materials 135(2) (1985) 190-196.
[35] G. Gutierrez, C. Onofri, S. Miro, M. Bricout, F. Leprêtre, Effect of ballistic damage in UO2 samples under ion beam irradiations studied by in situ Raman spectroscopy, Nuclear Instruments and Methods in Physics Research Section B: Beam Interactions with Materials and Atoms 434 (2018) 45-50.
[36] V.G. Keramidas, W.B. White, Raman spectra of oxides with the fluorite structure, The Journal of Chemical Physics 59(3) (1973) 1561-1562.
[37] T. Livneh, Coupling of multi-LO phonons to crystal-field excitations in UO2studied by Raman spectroscopy, Journal of Physics: Condensed Matter 20(8) (2008) 085202.
[38] H. He, D. Shoesmith, Raman spectroscopic studies of defect structures and phase transition in hyper-stoichiometric UO2+x, Physical Chemistry Chemical Physics 12(28) (2010) 8109-8118.
[39] L. Desgranges, G. Guimbretière, P. Simon, C. Jegou, R. Caraballo, A possible new mechanism for defect formation in irradiated UO2, Nuclear Instruments and Methods in Physics Research Section B: Beam Interactions with Materials and Atoms 315 (2013) 169-172.
[40] R. Mohun, L. Desgranges, C. Jégou, B. Boizot, O. Cavani, A. Canizarès, F. Duval, C. He, P. Desgardin, M.F. Barthe, P. Simon, Quantification of irradiation-induced defects in UO2 using Raman and positron annihilation spectroscopies, Acta Materialia 164 (2019) 512-519.
[41] T. Livneh, E. Sterer, Effect of pressure on the resonant multiphonon Raman scattering in UO2, Physical Review B 73(8) (2006) 085118.
[42] C. Sabathier, L. Vincent, P. Garcia, F. Garrido, G. Carlot, L. Thome, P. Martin, C. Valot, In situ TEM study of temperature-induced fission product precipitation in UO2, Nuclear Instruments and Methods in Physics Research Section B: Beam Interactions with Materials and Atoms 266(12) (2008) 3027-3032.

[43] C. Onofri, C. Sabathier, C. Baumier, C. Bachelet, H. Palancher, M.J.J.o.N.M. Legros, Evolution of extended defects in polycrystalline Au-irradiated UO2 using in situ TEM: Temperature and fluence effects, 482 (2016) 105-113.
[44] M. Toulemonde, W.J. Weber, G. Li, V. Shutthanandan, P. Kluth, T. Yang, Y. Wang, Y. Zhang, Synergy of nuclear and electronic energy losses in ion-irradiation processes: The case of vitreous silicon dioxide, Physical Review B - Condensed Matter and Materials Physics 83(5) (2011).
[45] M. Toulemonde, E. Paumier, C. Dufour, Thermal spike model in the electronic stopping power regime, Radiation Effects and Defects in Solids 126(1-4) (1993) 201-206.
[46] M. Toulemonde, A. Benyagoub, C. Trautmann, N. Khalfaoui, M. Boccanfuso, C. Dufour, F. Gourbilleau, J.J. Grob, J.P. Stoquert, J.M. Costantini, F. Haas, E. Jacquet, K.O. Voss, A. Meftah, Dense and nanometric electronic excitations induced by swift heavy ions in an ionic CaF${}_{2}$ crystal: Evidence for two thresholds of damage creation, Physical Review B 85(5) (2012) 054112.
[47] A. Debelle, J.-P. Crocombette, A. Boulle, E. Martinez, B.P. Uberuaga, D. Bachiller-Perea, Y. Haddad, F. Garrido, L. Thomé, M. Béhar, How relative defect migration energies drive contrasting temperature-dependent microstructural evolution in irradiated ceramics, Physical Review Materials 2(8) (2018) 083605.
[48] H. Palancher, R. Kachnaoui, G. Martin, A. Richard, J.C. Richaud, C. Onofri, R. Belin, A. Boulle, H. Rouquette, C. Sabathier, G. Carlot, P. Desgardin, T. Sauvage, F. Rieutord, J. Raynal, P. Goudeau, A. Ambard, Strain relaxation in He implanted UO2 polycrystals under thermal treatment: An in situ XRD study, Journal of Nuclear Materials 476 (2016) 63-76.
[49] W.J. Weber, Thermal recovery of lattice defects in alpha-irradiated UO2 crystals, Journal of Nuclear Materials 114(2) (1983) 213-221.

Supplementary material

Influence of electronic energy deposition on the ionization-induced recovery processes in uranium dioxide

G. Gutierrez[1], M. Bricout[1], F. Garrido[2], A. Debelle[2], L. Roux[1], C. Onofri[3]*

[1] Université Paris-Saclay, CEA, Service de Recherches de Métallurgie Physique, 91191, Gif-sur-Yvette, France

[2] Laboratoire de Physique des 2 infinis Irène Joliot-Curie (IJCLab), Université Paris-Saclay, Orsay, France

[3] CEA, DES, IRESNE, DEC, Cadarache, F-13108 St Paul lez Durance, France

*Corresponding author

E-mail: gaelle.gutierrez@cea.fr

UO_2 microstructure evolution after low-energy ion irradiation

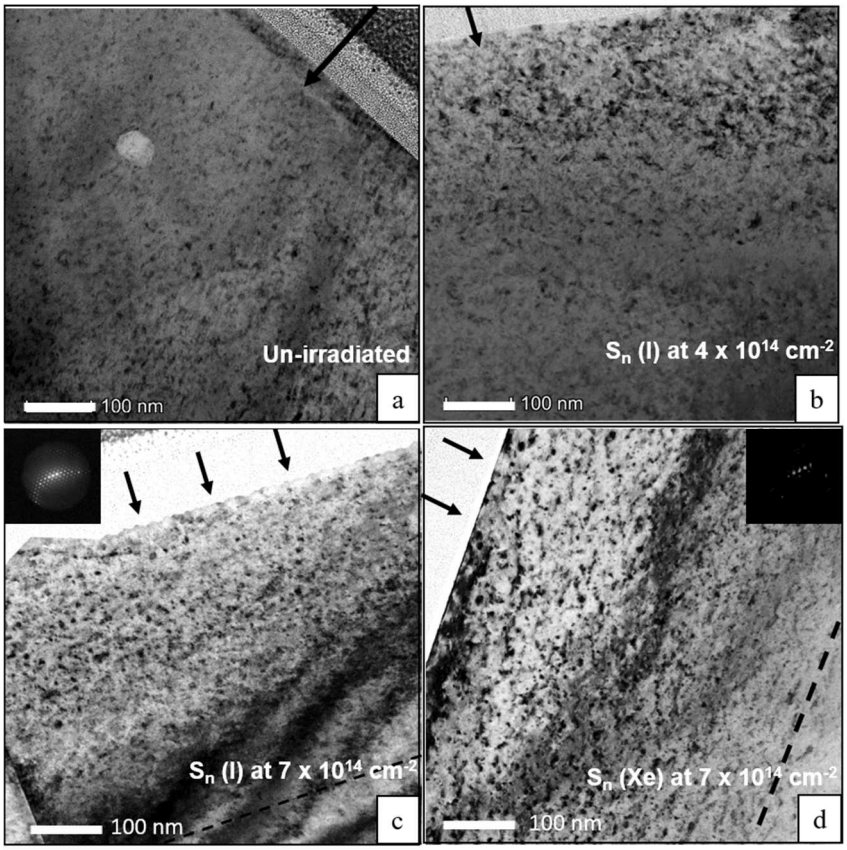

Figure S1 : Bright field TEM micrographs of (a) non irradiated sample and S_n(I) irradiated at (b) 4 x 10^{14} or (c) 7 x 10^{14} cm^{-2} and (d) S_n(Xe) at 7 x 10^{14} cm^{-2}. The diffraction vector is along <220>. The FIB lamella of an unirradiated sample presents dislocation loops, indicating a significant defect formation induced by the preparation method. No significant evolution is observed after the S_n(I) irradiation at 4 x 10^{14} cm^{-2} compared to the unirradiated one. With the ion fluence increase, the dislocation loop density increases.

A similar microstructure in term of dislocation loop size and density is observed for the S_n(I) and S_n(Xe) irradiation at a similar irradiation fluence.